NASA/TM—2011-217111

Radiation-Spray Coupling for Realistic Flow Configurations

Hossam El-Asrag
Massachusetts Institute of Technology, Cambridge, Massachusetts

Anthony C. Iannetti
Glenn Research Center, Cleveland, Ohio

October 2011

NASA STI Program . . . in Profile

Since its founding, NASA has been dedicated to the advancement of aeronautics and space science. The NASA Scientific and Technical Information (STI) program plays a key part in helping NASA maintain this important role.

The NASA STI Program operates under the auspices of the Agency Chief Information Officer. It collects, organizes, provides for archiving, and disseminates NASA's STI. The NASA STI program provides access to the NASA Aeronautics and Space Database and its public interface, the NASA Technical Reports Server, thus providing one of the largest collections of aeronautical and space science STI in the world. Results are published in both non-NASA channels and by NASA in the NASA STI Report Series, which includes the following report types:

- TECHNICAL PUBLICATION. Reports of completed research or a major significant phase of research that present the results of NASA programs and include extensive data or theoretical analysis. Includes compilations of significant scientific and technical data and information deemed to be of continuing reference value. NASA counterpart of peer-reviewed formal professional papers but has less stringent limitations on manuscript length and extent of graphic presentations.

- TECHNICAL MEMORANDUM. Scientific and technical findings that are preliminary or of specialized interest, e.g., quick release reports, working papers, and bibliographies that contain minimal annotation. Does not contain extensive analysis.

- CONTRACTOR REPORT. Scientific and technical findings by NASA-sponsored contractors and grantees.

- CONFERENCE PUBLICATION. Collected papers from scientific and technical conferences, symposia, seminars, or other meetings sponsored or cosponsored by NASA.

- SPECIAL PUBLICATION. Scientific, technical, or historical information from NASA programs, projects, and missions, often concerned with subjects having substantial public interest.

- TECHNICAL TRANSLATION. English-language translations of foreign scientific and technical material pertinent to NASA's mission.

Specialized services also include creating custom thesauri, building customized databases, organizing and publishing research results.

For more information about the NASA STI program, see the following:

- Access the NASA STI program home page at *http://www.sti.nasa.gov*

- E-mail your question via the Internet to *help@sti.nasa.gov*

- Fax your question to the NASA STI Help Desk at 443–757–5803

- Telephone the NASA STI Help Desk at 443–757–5802

- Write to:
  NASA Center for AeroSpace Information (CASI)
  7115 Standard Drive
  Hanover, MD 21076–1320

NASA/TM—2011-217111

Radiation-Spray Coupling for Realistic Flow Configurations

Hossam El-Asrag
Massachusetts Institute of Technology, Cambridge, Massachusetts

Anthony C. Iannetti
Glenn Research Center, Cleveland, Ohio

National Aeronautics and
Space Administration

Glenn Research Center
Cleveland, Ohio 44135

October 2011

This report contains preliminary findings, subject to revision as analysis proceeds.

Level of Review: This material has been technically reviewed by technical management.

Available from

NASA Center for Aerospace Information
7115 Standard Drive
Hanover, MD 21076–1320

National Technical Information Service
5301 Shawnee Road
Alexandria, VA 22312

Available electronically at http://www.sti.nasa.gov

Radiation-Spray Coupling for Realistic Flow Configurations

Hossam El-Asrag
Massachusetts Institute of Technology
Cambridge, Massachusetts 02139

Anthony C. Iannetti
National Aeronautics and Space Administration
Glenn Research Center
Cleveland, Ohio 44135

Abstract

Three Large Eddy Simulations (LES) for a lean-direct injection (LDI) combustor are performed and compared. In addition to the cold flow simulation, the effect of radiation coupling with the multi-physics reactive flow is analyzed. The flamelet progress variable approach is used as a subgrid combustion model combined with a stochastic subgrid model for spray atomization and an optically thin radiation model. For accurate chemistry modeling, a detailed Jet-A surrogate mechanism is utilized. To achieve realistic inflow, a simple recycling technique is performed at the inflow section upstream of the swirler. Good comparison is shown with the experimental data mean and root mean square profiles. The effect of combustion is found to change the shape and size of the central recirculation zone . Radiation is found to change the spray dynamics and atomization by changing the heat release distribution and the local temperature values impacting the evaporation process. The simulation with radiation modeling shows wider range of droplet size distribution by altering the evaporation rate. The current study proves the importance of radiation modeling for accurate prediction in realistic spray combustion configurations, even for low pressure systems.

1 Introduction

All modern combustors must balance the need for stability and performance with the goals of efficiency and emissions reduction. The emissions from stationary as well as non-stationary gas turbines have a profound effect on the environment and the balance of the eco-system [1]. For example, green house gases like Carbon dioxide CO_2, water vapor H_2O, and methane CH_4 are primary by-products from the burning of fossil fuels in internal combustion and gas turbine engines. These gases contribute to the global warming effect by absorbing the sun infrared rays. Other important pollutants are CO and NO_x. While CO has known hazardous health effects, NO causes acid rain and depletes the ultra-violet protective layer known as the ozone layer [2]. Finally, hydrocarbon fuels under rich conditions generate soot, which is known for its carcinogenic precursors and associated organics [3,4]. A common technique to reduce emissions of NO_x, CO, soot, and unburned hydrocarbons is to operate at lean premixed conditions, which in return leads to stability problems [5–7]. For aircraft engines, this poses a safety concern and is therefore typically avoided. Modern engines for next generation supersonic transportation aircraft, however, face even more stringent emissions regulations. Because of the high cruise altitude of these aircrafts in the lower stratosphere, engine emissions contribute directly to depleting the ozone layer [8]. To meet this challenge, several techniques have been proposed that are based on essentially premixed combustion. Among these are lean- premixed-prevaporized combustion (LPP) and lean direct injection combustion (LDI [9]). The latter is the focus of the present study.

The numerical prediction of the emissions in each system is faced by many challenges [10,11]. Gas turbine engines operate under turbulent conditions using complex fossil fuels [12] that introduce a wide range of length and time scales [13]. The resolution of these scales usually require fine mesh [14], which can lead to costly computation. In addition, the production of pollutants usually involves a large number of chemical reactions that expands the numerical effort. Furthermore, the complexity of the system is exacerbated as most of gas turbine engines fuels are injected in the liquid phase. The breakup of the spray droplets and their subsequent evaporation is another complex process that is not well understood yet [15,16] and which might be inherently coupled with the formation of pollutant and other physical process such as radiation [17]. Therefore, efficient numerical tools are needed to simulate reactive multiphase flow in complex geometries under high Reynolds number turbulent conditions [18–20].

In the past decade, large eddy simulation (LES), has proved to be a promising tool for turbulent reactive flow simulations [20] using both structured [21–26] and unstructured meshes [27–30]. In the current work, the full single element Lean Direct Injection (LDI) combustor is simulated in the LES framework. The Lean Direct Injection configuration is a good candidate for low emissions gas turbine requirements, where the combined geometry of a swirler and a Venturi nozzle results in stable combustion with potentially ultra-low NO_x and soot emissions. Air is injected in a swirler and it mixes with the fuel droplets to atomize, break up aerodynamically and partially premix in the Venturi before entering the combustor. The combination of the swirler and the Venturi has proven to maximize the atomization performance and minimize pressure drop across the injector [31]. The Venturi nozzle also provides sufficient residence time for the fuel droplets to vaporize and mix uniformly with the swirled air droplets in a lean mixture.

Here, non-reactive and reactive multi-physics simulations will be shown for an LDI system [32–34]. The current paper presents simulations that couple the interaction of turbulence with the important physical processes such as spray dynamics, chemistry, and radiation in a realistic configuration. The combustor emission characteristics, radiation coupling, flow/flame interaction, as well as the spray characteristics will be shown and compared with experimental data. A description of the modeling approach is outlined in the next section.

For accurate chemistry modeling, a detailed Jet-A surrogate mechanism is utilized [35]. The number of species and reactions considered are 122 and 900, respectively. Jet-A is known to be a common fuel for gas turbine engines. In the context of LES, the detailed Jet-A surrogate mechanism will be introduced in the frame work of the flamelet approach [36].

2 Combustion and radiation modeling

The combustion model used is the flamelet/progress-variable (FPV) approach [37,38]. The FPV approach is based on the flamelet concept, which relates the species mass fractions and energy to the mixture fraction through the flamelet equations

$$\rho\frac{\partial\Phi}{\partial t} - \rho\frac{\chi}{2}\frac{\partial^2\Phi}{\partial Z^2} = \dot{\omega}\,, \tag{1}$$

where Z is the mixture fraction, ρ is the density, $\Phi = (T, y_i)^T$ is a vector that contains the species mass fractions y_i and the temperature T. $\dot{\omega}$ is the source-term vector and χ is the scalar dissipation rate, which represents the

local rate of molecular mixing and which is strongly impacted by the large scale turbulent mixing process. The steady laminar flamelet model (SLFM) tabulates the solution of Eq. (1) (without the unsteady term) as a function of the mixture fraction and the stoichiometric scalar dissipation rate χ_{st}. Hence an equation of state (EOS) relating reactive scalars to the mixture fraction and its dissipation rate is written as

$$\Phi = \mathcal{F}_{\chi,\Phi}\left(Z, \chi_{\mathrm{st}}\right) . \tag{2}$$

The solutions to the flamelet equations are characterized by the non-linear interaction between chemistry and transport. For increasing dissipation rate, the flame temperature decreases, which ultimately leads to extinction. In SLFM, only non-extinguished solutions of the flamelet equations are considered, which limits the applicability of the model. It was shown by Pierce and Moin [37], for example, that SLFM predicts too much heat release in the essentially non-reactive regions close to the nozzle for a flame that is aerodynamically stabilized by a recirculation region. To overcome this limitation, Pierce and Moin [37] proposed a tabulation based on a reaction progress parameter λ instead of the scalar dissipation rate, which leads to the Flamelet/Progress Variable (FPV) formulation of the steady flamelet model.

As a result, the new state vector is given as $\Psi = \mathcal{F}_{\lambda,\Psi}\left(Z, \lambda\right)$. The reaction progress parameter λ is defined according to Ihme et al. [38] through a reaction progress variable C such that it is independent of the mixture fraction$Z$. The progress variable C can be a combination of certain species representing combustion products, temperature or sensible enthalpy. The progress variable here is the sum of the mass fractions of CO_2, CO, H_2O, and H_2. The reaction progress parameter λ is then defined for each flamelet as the stoichiometric

value of the reaction progress variable. Hence, the reaction progress parameter an be obtained from an inversion of the flamelet library.

$$C = \mathcal{F}_C\left(Z, \lambda\right) , \tag{3}$$

assuming that inversion is unique, which puts a restriction on the definition of the reaction progress variable.

The state vector $\Phi = \mathcal{F}_{\lambda,\Phi}\left(Z, \lambda\right)$ is obtained by the solution of Eq. (1), which includes all possible steady state solutions. Then, a joint probability density function (PDF) needs to be evaluated to obtain the Favre filtered ($\tilde{}$) values of the state vector. Since Z and λ are defined to be independent variables, by using Bayes$'$ theorem, the joint PDF at a certain time and position in space is given as

$$\tilde{P}\left(Z, \lambda; \mathbf{x}, \mathbf{t}\right) = \tilde{P}\left(\lambda | Z; \mathbf{x}, \mathbf{t}\right) \tilde{P}\left(Z; \mathbf{x}, \mathbf{t}\right) , \tag{4}$$

where marginal PDF of the mixture fraction $\tilde{P}\left(Z\right)$ is assumed to be a beta distribution [37], and the conditional reaction progress parameter PDF is a delta function. Since the β-distribution is characterized by the scalar mean $\widetilde{Z}$ and the scalar variance $\widetilde{Z''^2}$, and the delta-function by the mean $\widetilde{\lambda}$ the flamelet tabulation can be written in the form:

$$\widetilde{\Phi} = \mathcal{F}_{\widetilde{\lambda,\Phi}}\left(\widetilde{Z}, \widetilde{Z''^2}, \widetilde{\lambda}\right) . \tag{5}$$

With Eq. 5 and

$$\widetilde{C} = \mathcal{F}_{\widetilde{\lambda,\Phi}}\left(\widetilde{Z}, \widetilde{Z''^2}, \widetilde{\lambda}\right) , \tag{6}$$

the mean reaction progress parameter as an independent parameter in the tabulation can be replaced by $\widetilde{C}$, which is readily available in a simulation through the solution of a filtered transport equation for $\widetilde{C}$. As previously mentioned, for accurate temperature predictions, radiation might have to be considered. Ihme and Pitsch [39] have extended the above FPV approach to account for radiation as an unsteady process. In this model, the unsteady flamelet equations are solved considering radiative heat losses. The unsteady solution starts from the steady adiabatic solution and proceeds until a new steady state is found. The time can be replaced by the enthalpy, which is defined to include the heats of formation, and which therefore appears as a new parameter in the tabulation. Consequently, the extended FPV EOS can be written as

$$\widetilde{\Omega} = \mathcal{F}_{\widetilde{\Omega}}\left(\widetilde{Z}, \widetilde{Z''^2}, \widetilde{C}, \widetilde{H}\right) . \tag{7}$$

As a result, four parameters have to be computed as part of the LES solution, namely the filtered mixture fraction $\widetilde{Z}$, the subfilter scalar variance $\widetilde{Z''^2}$, the filtered progress variable $\widetilde{C}$, and the filtered enthalpy $\widetilde{H}$. Here, the scalar variance $\widetilde{Z''^2}$ is evaluated using an algebraic model [37], which assumes homogeneity and local equilibrium for the subgrid scales and is given by

$$\bar{\rho}\widetilde{Z''^2} = C_Z \Delta^2 \bar{\rho} |\nabla \widetilde{Z}|^2 , \tag{8}$$

where the mixture fraction coefficient C_Z is computed dynamically and $\bar{\rho}$ is the filtered density. Finally, three additional transport equations are solved for $\widetilde{Z}$, $\widetilde{H}$ and $\widetilde{C}$ as follows:

$$\frac{\partial \bar{\rho}\widetilde{Z}}{\partial t} + \nabla \cdot \left(\bar{\rho}\widetilde{u}\widetilde{Z}\right) = \nabla \cdot \left(\bar{\rho}\widetilde{D}\nabla\widetilde{Z}\right) + \nabla \cdot \widetilde{\tau}_z^{res} , \tag{9}$$

$$\frac{\partial \bar{\rho}\widetilde{C}}{\partial t} + \nabla \cdot \left(\bar{\rho} u \widetilde{C}\right) = \nabla \cdot \left(\bar{\rho}\widetilde{D}\nabla\widetilde{C}\right) + \nabla \cdot \widetilde{\tau}_c^{res} + \bar{\rho}\widetilde{\dot{\omega}}_C \,, \tag{10}$$

$$\frac{\partial \bar{\rho}\widetilde{H}}{\partial t} + \nabla \cdot \left(\bar{\rho} u \widetilde{H}\right) = \nabla \cdot \left(\bar{\rho}\widetilde{D}\nabla\widetilde{H}\right) - \widetilde{\dot{q}}_r \,, \tag{11}$$

where $\widetilde{D}$ is the filtered molecular diffusivity, assuming equal species diffusivities and unity Lewis numbers, and $\widetilde{\dot{\omega}}_C$ is the filtered chemical source term of the progress variable, which is tabulated in the flamelet library. In the above equations, the residual stresses $\widetilde{\tau}^{\text{res}}$ are modeled by a dynamic approach [37]. For an optically thin radiation model [40], the filtered radiation source term is

$$\widetilde{q}_r = 4\sigma \left(\widetilde{\mathcal{T}^4} - \widetilde{\mathcal{T}}_\infty^4\right) \sum(\widetilde{\mathbf{p_i}\mathbf{a_i}}) \,, \tag{12}$$

where $\mathbf{p_i}$ and $\mathbf{a_i}$ are the partial pressure and Planck mean absorption coefficient of species i, respectively, σ is the Stefan Boltzmann constant, and $\widetilde{\mathcal{T}}_\infty^4$ is the ambient reference temperature at one atmosphere. To account for the unsteadiness of NO_x production, the filtered mass fraction of NO, $\widetilde{Y}_{\text{NO}}$ is computed by solving a transport equation rather than extracting the values from the flamelet tables [39]. The filtered LES equation can then be written as

$$\frac{\partial \bar{\rho}\widetilde{Y}_{\text{NO}}}{\partial t} + \nabla \cdot \left(\bar{\rho} u \widetilde{Y}_{\text{NO}}\right) = \nabla \cdot \left(\bar{\rho}\widetilde{D}\nabla\widetilde{Y}_{\text{NO}}\right) + \bar{\rho}\widetilde{\dot{\omega}}_{\text{NO}} \,, \tag{13}$$

where the filtered production rate $\widetilde{\dot{\omega}}_{\text{NO}}$ is closed according to the model by Ihme and Pitsch [39]. More details about the FPV and the radiation model can be found in [39].

3 Secondary breakup spray model

Jet-A fuel spray droplets are injected from the centerline simplex atomizer, with a specified drop-size distribution. The hollow cone spray has a total angle of 90°. The spray models employed have been described in detail by Apte et al. [41,28,42]. Here, we summarize the most important features.

A stochastic subgrid model for spray atomization is used here. The initial liquid film is approximated by a droplet of size equal to the nozzle diameter. The model views the subsequent particle breakup of the injection of a specified drop-size as a discrete random process, where droplet size is treated as a time-dependent stochastic variable. The temporal and spatial evolution of the particle size distribution is then governed by the Fokker-Plank differential equation. This evolution leads to the formation of new droplets and destruction of the parent ones. The new droplets position and velocity vectors are tracked by a Lagrangian algorithm in the physical space. Two-way coupling between the gas phase and the liquid droplets is achieved by the source terms in the gas-phase equations, which represent the mutual effect of mixing and momentum/energy transport. These effects are induced by droplet breakup, evaporation, and convection by the flow-field. Simultaneously with the process of secondary droplet breakup and mixing with the gas phase, the liquid phase evaporates under the appropriate conditions. The evaporation model solves a set of ordinary differential equations (ODEs) that describe the variation of the droplet mass and temperature due to evaporation and assumes that non-equilibrium effects inside the droplet volume are neglected. A third-order Runge-Kutta scheme is used to integrate the set of ODEs with the minimum physical drop time scale. The mathematical formulation of the above scheme is omitted here for brevity and can be found elsewhere [42].

4 Numerical setup

The simulation is performed by the unstructured LES code CDP. CDP is a set of massively parallel unstructured finite-volume flow solvers developed specifically for large eddy simulation. The solver used to perform the reactive simulations reported in this work is a node-based low-Mach number solver [43]. A the fully incompressible solver is used for the non-reactive case for computational efficiency. The LES governing equations and the sub-grid momentum closures are omitted here for brevity.

The experimental setup and data are provided by Farhad et al. [44]. The geometry of the single-element combustor is shown in Fig. 1a with the inflow pipe upstream of the swirler. Liquid fuel is injected through the center (closed for the non-reactive case), while air is injected through a swirler with vane angles of 60°. The global swirl number is 1. The swirler is composed of six helical vanes with an effective area of 870 mm^2. The fuel droplets from the centerline and the swirled air are mixed in a converging-diverging Venturi nozzle. The helical air swirler has an inside diameter of 9.3 mm and an outside diameter of 22.1 mm. The combustor has a square cross-sectional area of 50.8 x 50.8 mm.

The mesh uses 1,072,640 hexahedral elements, which is slightly above the $861,823$ element mesh used in the RANS calculations [44,45] and about half the LES structured mesh used by Patel and Menon [22]. The unstructured mesh is shown in Fig. 1. The mesh distribution along the $z = 0$ plane and in the vanes is shown in Fig. 1b, while the $y - z$ plane grid distribution

is presented in Fig. 1c. The mesh cells are clustered toward the centerline and toward the walls of the combustor. Here, we extend the original RANS mesh [44] to account for more realistic inflow.

An inflow bulk velocity of 20.14 m/s is provided through a tube upstream of the swirl injector. The inflow air is at temperature $T_o = 294\,\mathrm{K}$ and pressure of 1 atm, while the global equivalence ratio is 0.75. The fuel spray has an inflow mass flow rate of 4.15.10−04 kg/s and an initial velocity of 20 m/s. The droplets are injected with a Rosin-Rammler distribution

$$F_m(D) = 1 - \exp\left(-\left(\frac{\mathrm{D}}{\delta}\right)^{\mathrm{n}}\right), \tag{14}$$

where $F_m(D)$ is the cumulative distribution function of the droplet diameter D, and the parameters $n = 1.34$ and $\delta = 24\ \mu\,\mathrm{m}$ are chosen to curve-fit the distribution of the experimental data at the first measured location (x = 3mm). An inflow recycling technique is used [46] to achieve realistic inflow turbulence. The recycling is done until the inflow profile of the upstream pipe recovers a realistic inflow turbulent boundary layer. The boundary conditions used are inflow/outflow in the x-direction and adiabatic walls in the y and z directions.

Statistics are collected over a physical time of 0.032 seconds after the initial transient for the reactive flow cases and over 0.167 seconds for the cold-flow case. Based on the bulk inflow velocity and the full length of the combustor, this represents two complete flow-through times for the reactive cases and about seven flow-through times for the non-reactive case. The simulation was performed on a Linux cluster at Stanford University with infiniband interconnection and dual Intel Clovertown (Quad Core) 2.33 GHz processors with 8 GB

RAM per node. With the current mesh resolution the code scaling was found to level off at 96 processors for the spray-combustion case. The computational time per flow through time was 900 CPU hours for the reactive case.

5 Results and discussion

In this section, two LES simulations are compared to the experimental data. The statistics for the two simulations, with and without radiation, are collected over the same total run time. Unless mentioned otherwise, only the case with radiation is considered for the comparison with the radial experimental profiles. Almost all available experimental data are used in the comparison and selected non-reactive flow data are included to show the effect of heat release.

First, the time-averaged flow features of the reactive flow will be shown and compared with the non-reactive case with an emphasis on the radiation effect. Subsequently, the mean and root mean squared (rms) values of the gas flowfield, the scalars, and the spray characteristics will be compared with the experimental data.

Due to the swirling flow, an adverse pressure gradient is generated in the axial direction and a vortex breakdown bubble (VBB) is established. The LDI is characterized by a central recirculation zone (CRZ) in addition to recirculation zones (RZs) at the corner of the dump plane. Three RZs had been observed previously in the non-reactive case [46,47,45]. Figures 2a and 2b show isosurfaces of mean axial velocity for $\langle \overline{U} \rangle = 0\,\mathrm{m/s}$ for both the reactive and non-reactive cases, where the brackets denote a time average. The length of the CRZ in the non-reactive case is approximately twice as that in the

reactive one. However, the reactive CRZ has a larger effective bulk diameter. Also, a small toroidal RZ close to the divergent part of the Venturi exists in the reactive flow case as shown by the side view in Fig. 3, which is caused by flow separation. A more compact and stronger reactive CRZ is due to the expansion of the flowfield by heat release effects as shown later.

Figure 4 shows vector plots for the time-averaged total velocity magnitude for the reactive flow case with radition. Only the projections in the $y = 0$ plane are shown here for clarity. Figure 4a shows that the CRZ starts early inside the divergent part of the Venturi nozzle, in addition to a small RZ observed just downstream of the injector exit. These two small RZs inside the Venturi enhance mixing and atomization of the spray with the swirling air. However, at the injector exit, the droplets and the spray sheet have enough momentum to penetrate this RZ toward the Venturi exit as shown in Fig. 4b. This observation will be confirmed later by the axial and radial velocity profiles. Figure 4c shows the velocity magnitude vector plot downstream of the dump. The CRZ has an azimuthal vortex at the location $x = 17\,\mathrm{mm}$ downstream of the dump plane. Figure 4c also shows an additional annular vortex at the burner corners where the second RZ is located. Corner vortices are found to extend along the combustor wall corners up to the exit plane in the $y - z$ plane (not shown here), which will affect the spray distribution as shown later.

An instantaneous temperature distribution is shown in Fig. 5. Figure 5a shows a snapshot of the $y = 0$ plane. Figures 5b-d show three consecutive snapshots at the location $x = 11$ mm. Figures 5a and 5d are at the same instant in time. The temperature shows high gradients at the shear layer location and around the CRZ, which leads to strong mixing. At the edge of the CRZ, fresh cold gases (dark areas) are engulfed into the CRZ. Inside the core of the RZ, the

temperature shows nearly uniform distribution due to the strong mixing the fluid undergoes before entering the CRZ.

A comparison of the heat release distribution is shown in Fig. 6. The flame without radiation shows locally lower mean values than the case with radiation, for which the heat release is more distributed. The reason is that radiation causes the temperatures to be locally lower, which leads to smaller evaporation rates of the liquid fuel and consequently a lower fuel vapor mass fraction as observed in Fig. 7.

Two snapshots of the spray distribution from the two simulations are shown in Fig. 8. The spray exhibits a 90^o cone angle. Some of the spray droplets are trapped inside the corner vortex, which results in an increase in the mean droplet diameter close to the walls. The simulation with radiation shows a wider range of droplet sizes. For the shown instantaneous snapshots with radiation, droplet size ranges between $0.5\,\mu$m and $50\,\mu$m, while without radiation the range is between $0.7\ \mu$m and $40\,\mu$m. This is attributed to a higher evaporation rate when radiation is not included. Since no primary breakup model is employed here, the spray spectrum shows an intermediate regime, where the spray injected from the nozzle undergoes secondary breakup, followed by a dilute regime where the droplets evaporate. The intermediate regime is mainly inside the Venturi, while the dilute regime extends until all the droplets are evaporated.

The steady state droplet and parcel-size histograms for the whole combustor volume for both cases are shown in Fig. 9. In general, the case without radiation has a lower number density of droplets over the whole spectrum. This will subsequently affect the flow dynamics and the flame structure (as shown

earlier). The radiation effect on droplet evaporation can be assessed in Fig. 10. This figure shows the time-averaged rate of droplet mass evaporation at the plane $y = 0$. This value represents the time average of the source term of the droplet mass variation. The case without radiation shows higher evaporation rates in the vicinity of the injector and in the flame surface surrounding area due to the reasons discussed earlier.

The LES simulation with radiation modeling is compared with the experimental data next. Figures 11a and 11b show spray droplet mean diameter D_{10} and Sauter mean diameter D_{32}. Overall good agreement is observed. At the first three axial locations a peak value is shown that starts at a radial distance of 8 mm from the centerline (for $x = 3$ mm) and then spreads radially towards the wall (for $x > 3$ mm). This location is an indication of the spray sheet cone angle. Since the spray droplets directly emitted from the injector have a large droplet size, the profiles show peak values at these radial locations. Downstream of $x = 15$ mm some droplets are trapped in the wall-corner vortex. It is interesting to note that the value of the mean diameter is increasing downstream due to evaporation of the smaller diameter droplets (larger than the cut-off value of the experimental measurements). This is consistent with the experimental data.

The spray droplets$'$ mean axial velocity distribution is shown in Fig. 12. Good agreement is observed for all locations. Consistent with Fig. 11, the LES shows over-predicted droplet mean axial velocity at the locations of over-prediction in the droplet size. Again, over-prediction is expected at the first few locations, where the small-size droplets are not considered in the experiment.

To show the extent of the centerline RZ and the effect of heat release and radiation on the flow features, the centerline mean axial velocity profiles are shown in Fig. 13. Reactive and non-reactive data from experiments are compared with the LES results with and without radiation. The figure shows that the non-reactive RZ extends to about 100 mm downstream of the dump, while the reactive RZ is stronger and more compact (about 50 mm in length). The expansion of the flow by heat release changes the local velocity and pressure distribution. This local expansion (in the flame region) increases the pressure gradient and leads to faster flow deceleration. This results in a shorter but wider RZ. The CRZ without radiation is over-predicted by about 5 mm due to the change in the flame structure and the spray distribution as shown in Fig. 6.

As discussed below, the LES simulation shows that inside the divergent section of the Venturi a small RZ is established, followed by an increase in the velocity due to a sudden expansion after the dump. This is followed by a steep reduction inside the RZ due to the adverse pressure gradient. There are no experimental data inside the Venturi, but the profile captures the initial peak after the dump accurately, which confirms the foregoing physical conclusions. Note that the current simulation captures the centerline profile initial peak. The deviations near the injector will be discussed later.

The mean and rms axial velocities are shown in Figs. 14 and 15. The first three locations ($x = 3$ mm, $x = 5$ mm and $x = 9$ mm) are found to be the most difficult to match with the experiment. These locations exhibit high unsteadiness and high measurement errors. The experimental measurements [34] use a Phase Doppler Particle Analyzer (PDPA). A problem usually related to the measurements is how to distinguish between the seed particles to measure the gas phase velocity and the spray droplets. In the LDI experimental mea-

surements [34] the nominal diameter of the seed particles used was 1 μm. To distinguish between the spray and the seed particles, all particles smaller than 4 μm were used to represent the gas-phase velocity. However, inside the CRZ the small spray droplets just ejected from the nozzle still have high momentum in the positive direction. As a result, the experimental velocity profiles near the exit (i.e., $x = 3$ mm, x= 5 mm and $x = 9$ mm) are all positive despite the existence of the CRZ. Therefore, at these locations we expect to underpredict the experimental data. A previous RANS simulation [45] shows also higher deviation at $x = 3$ mm, and comparable results at $x = 9$ mm. The LES simulation by Patel and Menon [22] also shows lower velocity at the location $x = 5$ mm. Starting from the $x = 15$ mm location, the current LES simulation shows good results compared with the experimental data. The CRZ extends to approximately 50 mm downstream of the dump. At the $x = 92$ mm location, the profile shows a nearly uniform velocity that recovers the inflow mass flow rate at the exit cross-sectional area. This uniformity is important in gas turbine engines to minimize the thermal stresses on the turbine blades. A slight deviation is found towards the walls. This can be attributed to the fact that the CRZ in the current simulation is wider than in the experiment. As a result, the flow is more compressed between the CRZ and the walls and the velocity is higher.

The rms axial velocity profile is shown in Fig. 16. The rms peaks close to the dump plane at the onset of the shear layer and then decays axially as the shear layer decays downstream. The predicted and experimental axial rms profiles show good agreement. The high rms values at the first three locations confirm the high unsteadiness of the shear layer. For example, at $x = 5$ mm the rms value is around 100% of the corresponding mean value. At the first

three locations, over-prediction is noticed at the $y = 15\,\text{mm}$ radial location. The discrepancy with the experimental data at the first three locations is due to the reasons mentioned in the previous paragraph. The LES data predict two rms peaks that start at the radial location $y = 9\,\text{mm}$ at the first axial location. These two peaks spread downstream with the spread of the shear layer. Downstream of $x = 20\,\text{mm}$, the peaks start to move again toward the centerline following the CRZ surface. After reaching the $x = 46\,\text{mm}$ location, the peaks are completely merged. After this location, no reverse flow exists and the shear layer is completely diffused. Similar observations apply to Fig. 17, where the radial profiles of the turbulent shear stress are plotted. The shear stress shows antisymmetric radial profiles. Good agrement is shown, with deviations at the first two locations. The zero shear stress at the centerline indicates flow symmetry around the centerline.

Figure 18 shows the mean velocity component in the y-direction at different axial locations. The flow is rotating in the clockwise direction (CCW) viewed from the outflow cross-section. The global swirl number is of the order of 1. In contrast to other velocity components, the results show good agreement with the first location at $x = 3\,\text{mm}$. The flow shows solid body rotation around the centerline downstream of the location $x = 29\,\text{mm}$. Upstream of this location the flow is rotating around the central RZ.

The focus of the following discussion are the LDI emission characteristics. For supersonic vehicles, the NO emissions directly deplete the stratospheric ozone layer. Therefore, accurate models are required to predict gas turbine emissions. As discussed earlier, NO production is a slow process and it is coupled with other processes that have long characteristic time scales such as radiation. Radiation affects NO in an indirect way through the change in temperature,

which then changes the production rate. As a result, the first step is to predict temperature accurately. Figure 19 shows the centerline mean temperature with and without radiation modeling. This figure shows that without radiation the temperature is over-predicted. This is consistent with earlier observations.

The radiation model employed here is an optically thin model [39]. The model assumes that the medium is non-absorbing and neglects the heat lost or gained by wall absorption and reflection. Figure 20 shows radial temperature profiles at the locations where experimental data are available. The temperature is under-predicted at the centerline. This may suggest a need for a more accurate radiation model that accounts for the absorption within the flame, the scattering by the media (although might be negligible in this case), and the wall effect.

Figure 21 shows the centerline species distribution for CO and NO. The CO level along the centerline is captured reasonably well. An initial peak is observed in the rich combustion region followed by a decay in the CO level as it is oxidized to produce CO_2. The centerline NO profile also shows good results. The effect of radiation generally improves the results.

6 Conclusions

Large eddy simulations for a liquid fuel injection LDI are performed. The simulations show that LDI is a good candidate for low emissions, yet stable, gas turbine engines. Radiation modeling is found to be essential for accurate NO and temperature predictions. By changing the heat release distribution, radiation alters the spray dynamics and the droplets size distribution. Thus,

radiation can be important even for low pressure systems where radiation from flame region is relatively small, but effect of radiation on spray dynamics significantly affects temperature distribution. The simulations show the current ability of LES as a numerical tool to simulate multi-physics problems in complex geometries using realistic chemistry models.

7 Acknowledgements

This work is funded by NASA Glenn Research Center. The authors thanks Nan-Suey Liu for providing advice, grid and experimental data for comparison. Many thanks to Heinz Pitch for his continuous support and revision for this manuscript and for his helpful discussions and technical advice. The authors also acknowledge Frank Ham from Stanford for his valuable support with the CDP code and Jeffrey P. Moder from GRC for reviewing the final version of the manuscript.

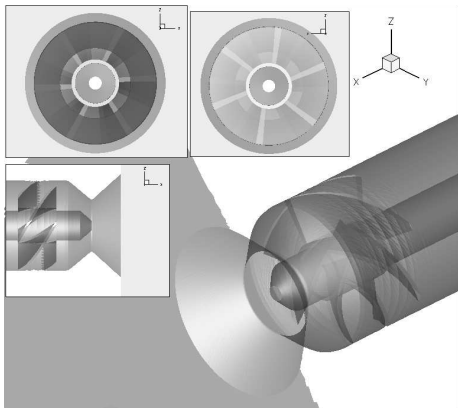

(a) LDI geometry

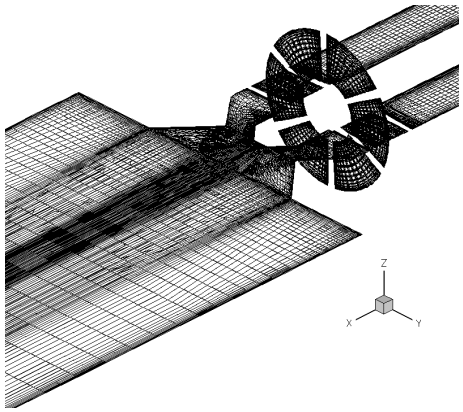

(b) The vanes and the y-x mesh plane

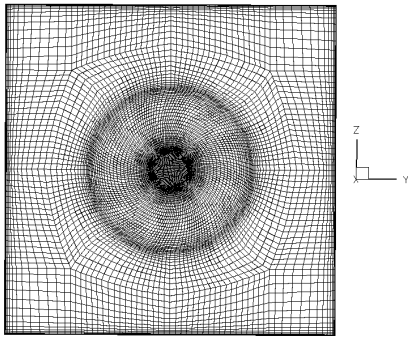

(c) y-z mesh plane

Fig. 1. The LDI single element geometry and unstructured hexahedral mesh.

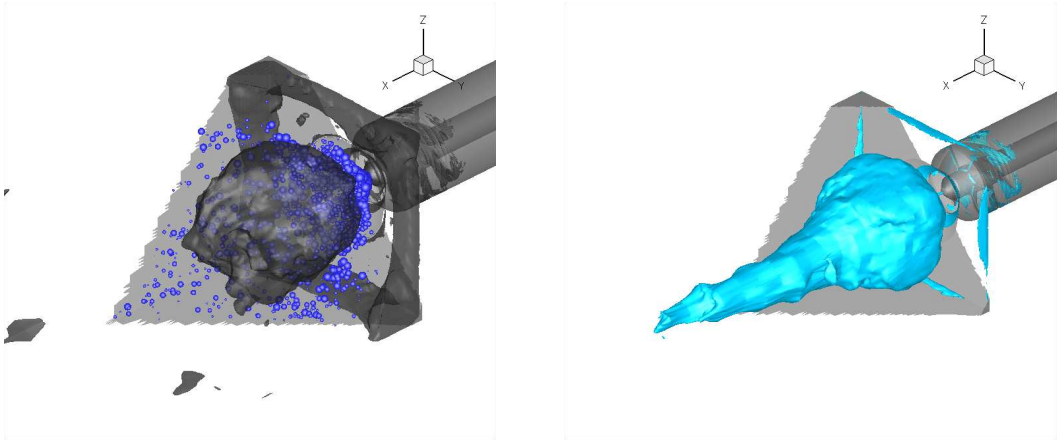

(a) Reactive (b) Non-reactive

Fig. 2. Iso-surface of the time-averaged axial velocity ($\langle \overline{U} \rangle = 0\,\mathrm{m/s}$).

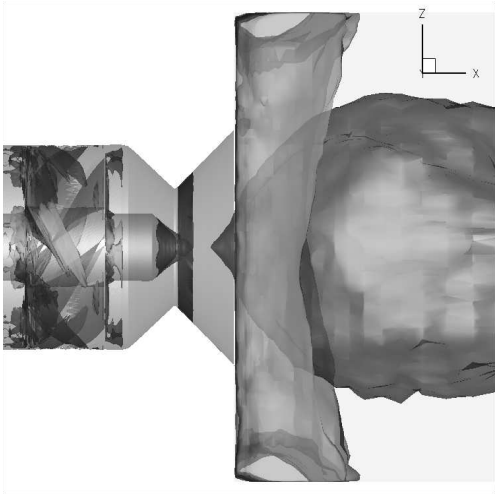

Fig. 3. Side view ($y = 0$ plane) to the CRZ for the reactive flow case.

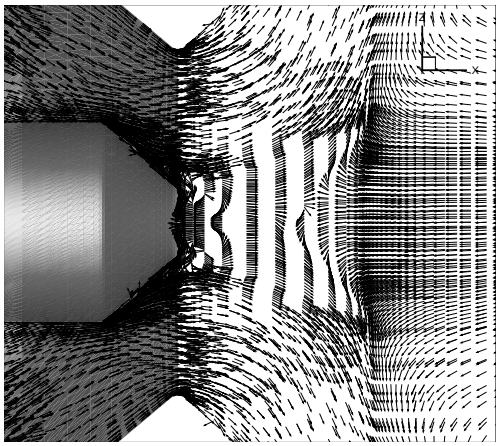

(a) Zoom of the injector area

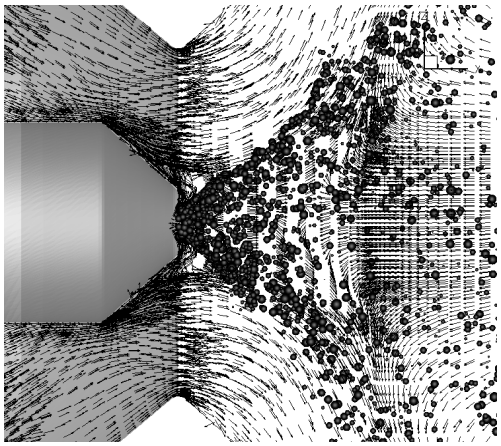

(b) Zoom of droplet distribution in the injector area

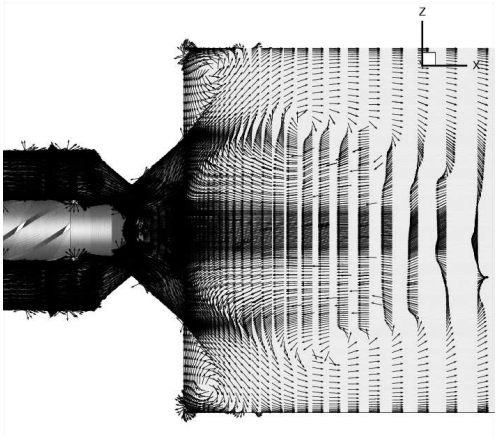

(c) The vortices around the CRZ and at the corners.

Fig. 4. Vector plots of the mean velocity magnitude projected in the $y = 0$ plane for the reactive flow case with radiation.

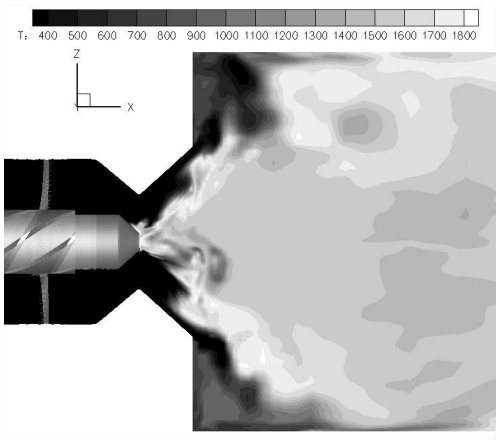

(a) $y = 0$ plane

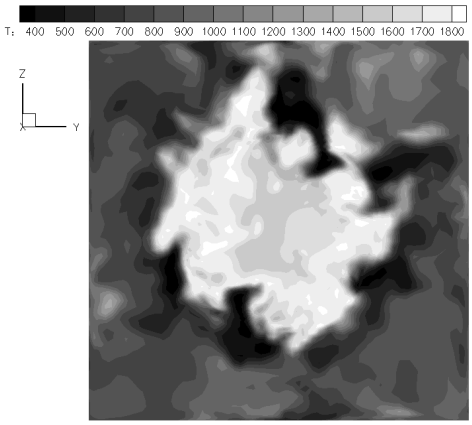

(b) z-y plane

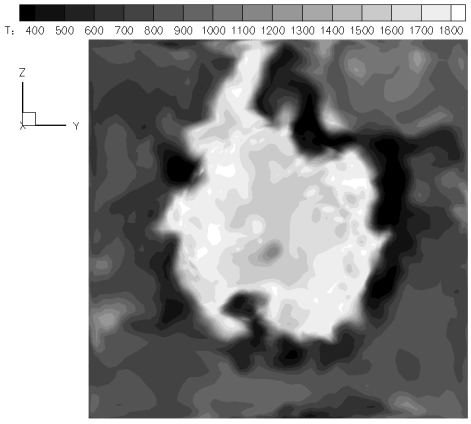

(c) z-y plane

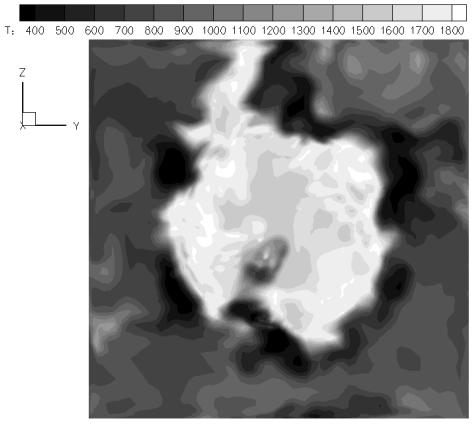

(d) z-y plane

Fig. 5. Instantaneous temperature distribution for the case with radiation. (a) for the z-x plane, (b), (c) and (d) for the z-y plane at three consecutive time snapshots at $x = 11$ mm.

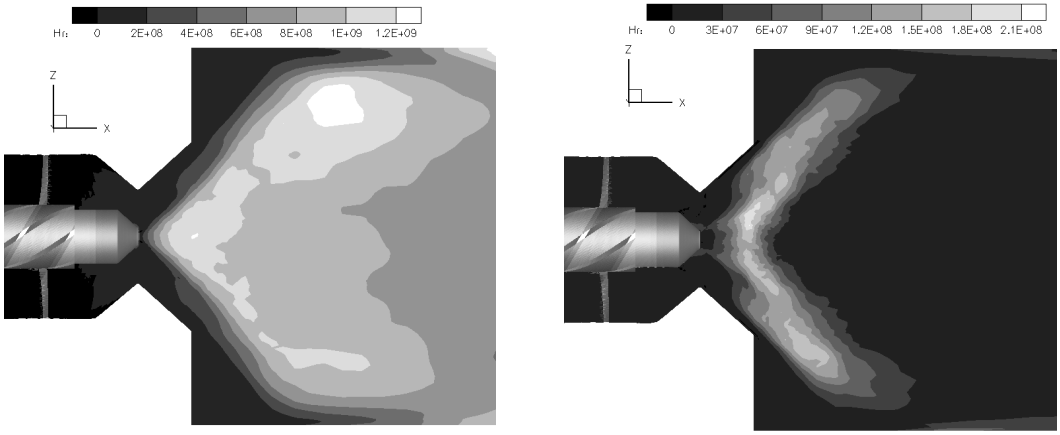

(a) With radiation (b) No radiation

Fig. 6. Distribution of the time averaged heat release $\langle \overline{Q}_{Hr} \rangle$.

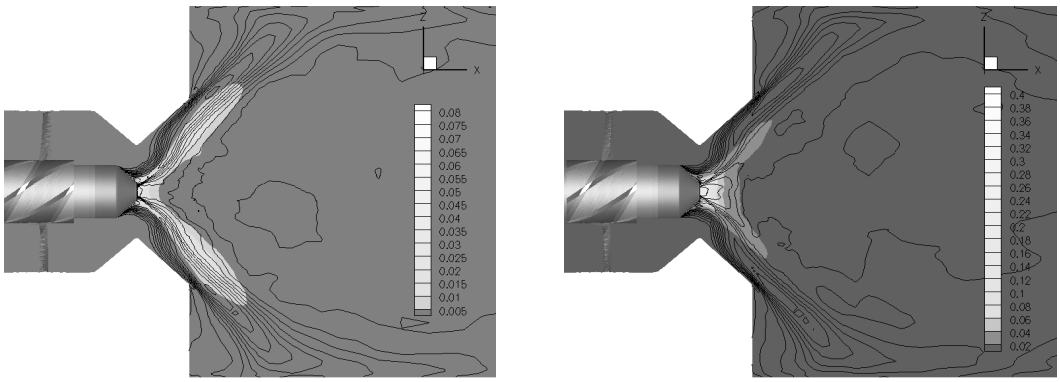

(a) With radiation (b) No radiation

Fig. 7. Cross sectional view through the swirler at $y = 0$ plane for distribution of the time-averaged gas-phase fuel mass fraction $\langle \overline{Y}_F \rangle$ combined with the RMS temperature contours (T_{rms}).

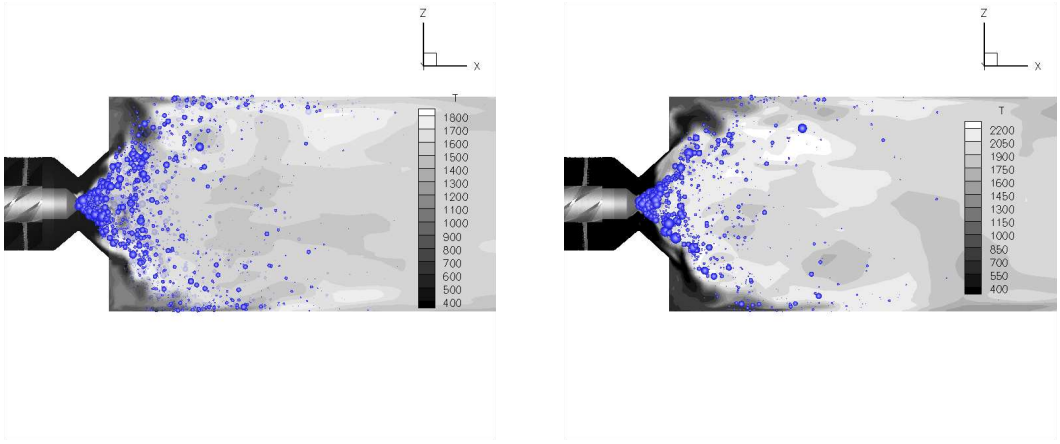

(a) With radiation (b) No radiation

Fig. 8. Instantaneous droplet distribution sized by droplet mass combined with the instantaneous temperature distribution at the $y = 0$ plane.

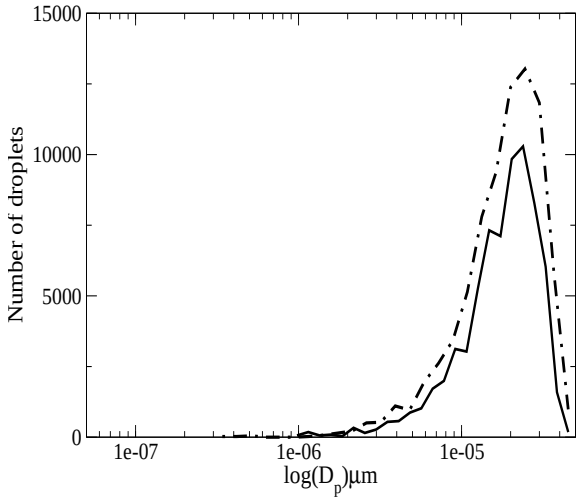

Fig. 9. Radiation effect on the droplet parcel histogram. (With radiation $- \cdot - \cdot -$, without radiation $-$)

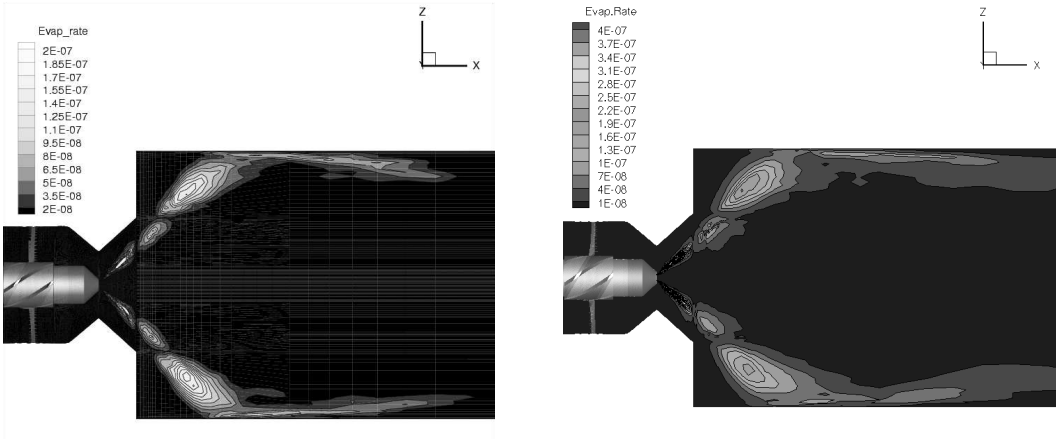

(a) With radiation (b) No radiation

Fig. 10. Time-averaged droplet mass evaporation rate in (kg/s) at the central $y = 0$ plane.

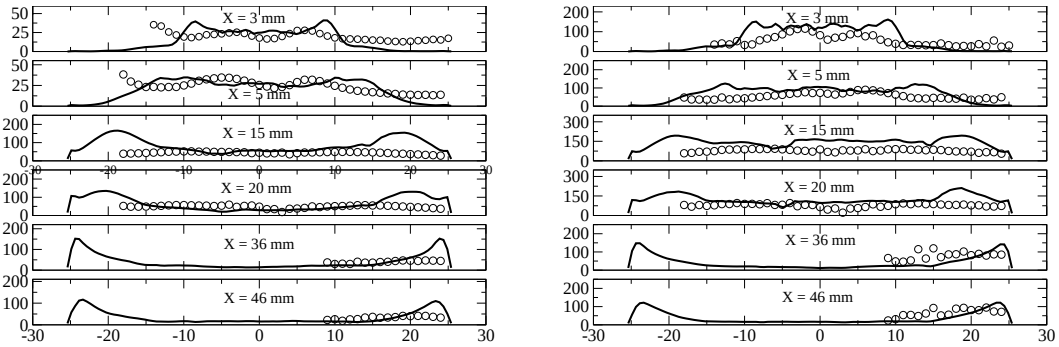

(a) Arithmetic mean droplet diameter (D_{10})

(b) Sauter mean diameter (SMD) (D_{32})

Fig. 11. Radial profiles of droplet arithmetic mean and Sauter mean diameters (Experiment data ∘, computation −)

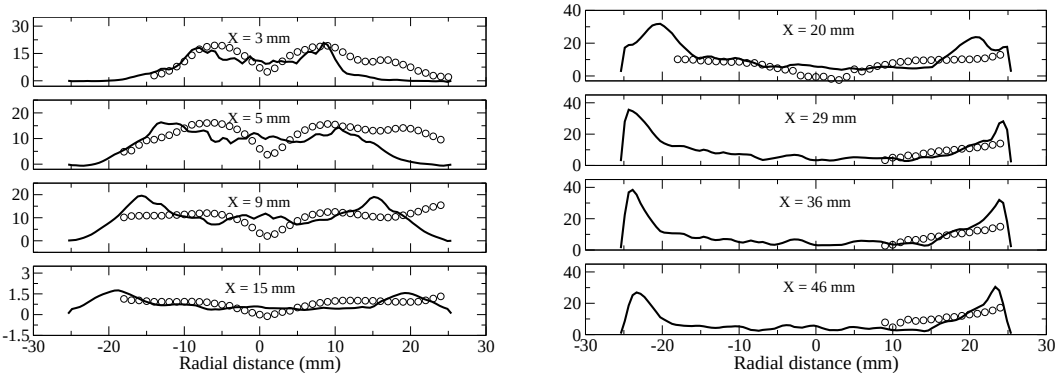

(a) $x = 3\,\text{mm}$-$x = 15\,\text{mm}$ (b) $x = 20\,\text{mm}$-$x = 46\,\text{mm}$

Fig. 12. Radial profiles of mean droplet axial velocity (Experiment data ∘, computation −)

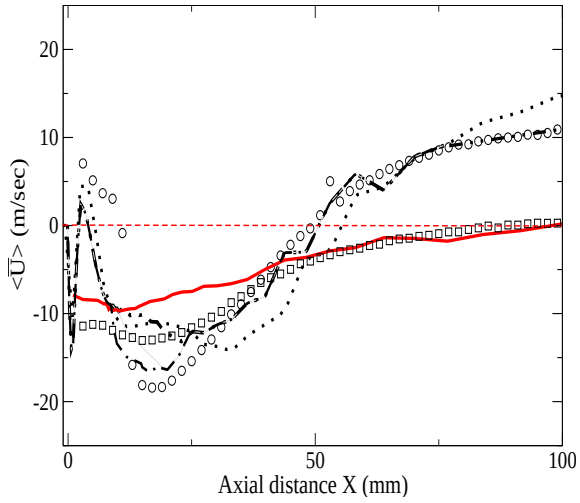

Fig. 13. Comparison of time-averaged centerline axial velocity $\langle \overline{U} \rangle$. Non-reactive flow (Experiment □, computation −), reactive flow (Experiment ∘, computation with radiation − · −, computation with no radiation ···).

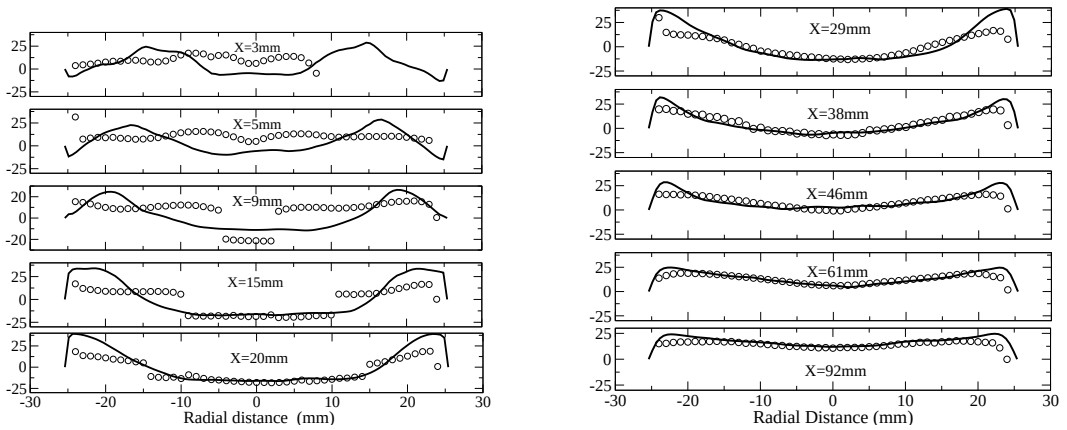

(a) $x = 3\,\mathrm{mm}$ - $x = 20\,\mathrm{mm}$ (b) $x = 29\,\mathrm{mm}$ - $x = 92\,\mathrm{mm}$

Fig. 14. Mean axial velocity $\langle \overline{U} \rangle$ at different axial locations (Experiment data $\circ$, computation $-$).

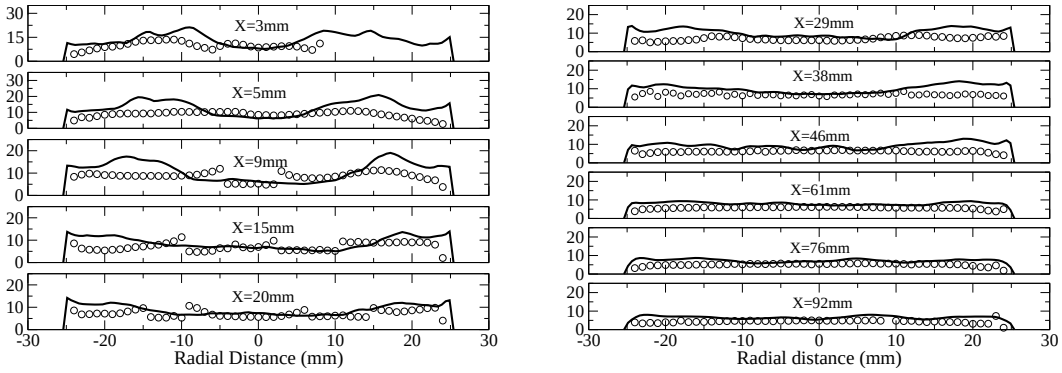

(a) $x = 3\,\text{mm}$-$x = 20\,\text{mm}$ (b) $x = 29\,\text{mm}$-$x = 92\,\text{mm}$

Fig. 15. RMS axial velocity U_{rms} at different axial locations (Experiment data $\circ$, computation $-$).

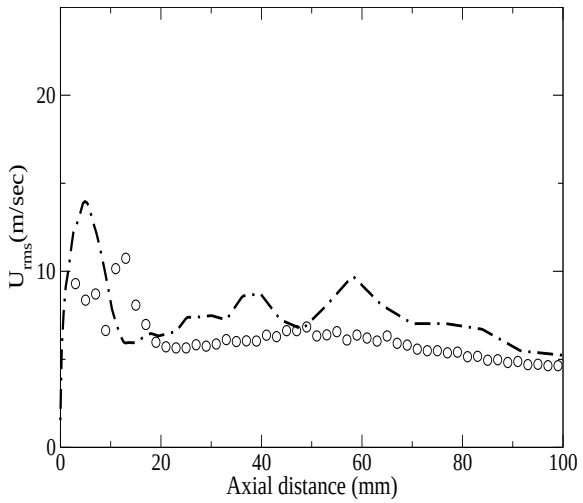

Fig. 16. RMS axial velocity along the centerline (Experiment data ∘, computation −).

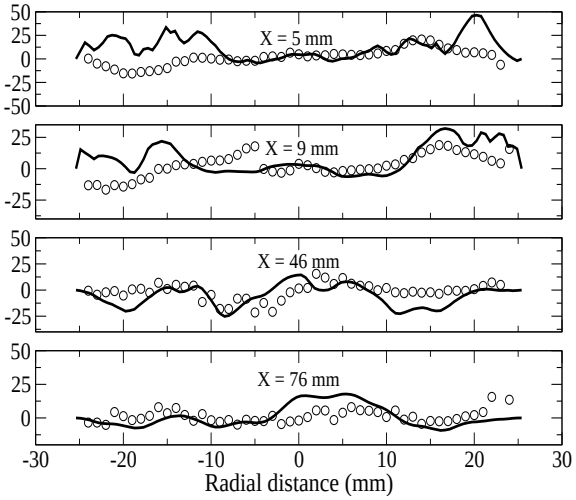

Fig. 17. Radial profiles of the shear stress $\widetilde{u'v'}$

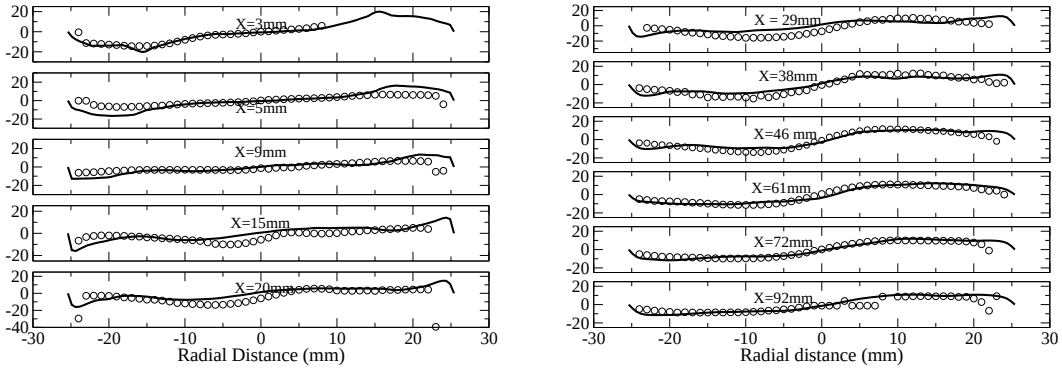

(a) $x = 3\,\text{mm}$-$x = 20\,\text{mm}$ (b) $x = 29\,\text{mm}$-$x = 92\,\text{mm}$

Fig. 18. Mean velocity component in the y direction $\langle\ \overline{U}_Y\ \rangle$ (Experiment data $\circ$, computation $-$)

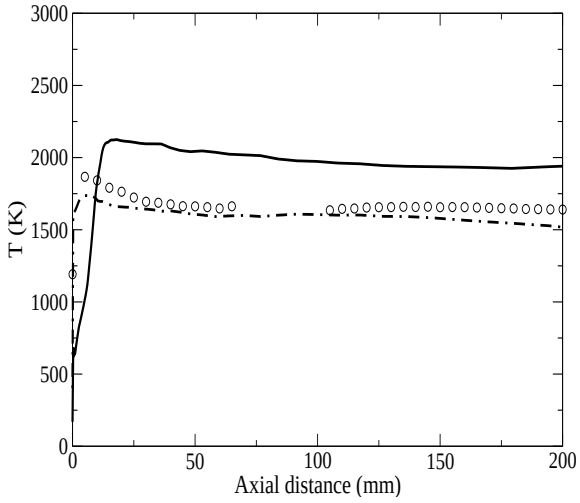

Fig. 19. Comparison of the centerline mean temperature $\langle \overline{T} \rangle$. (Experiment $\circ$, computation without radiation $(-)$ and with radiation $(\cdot - \cdot)$.

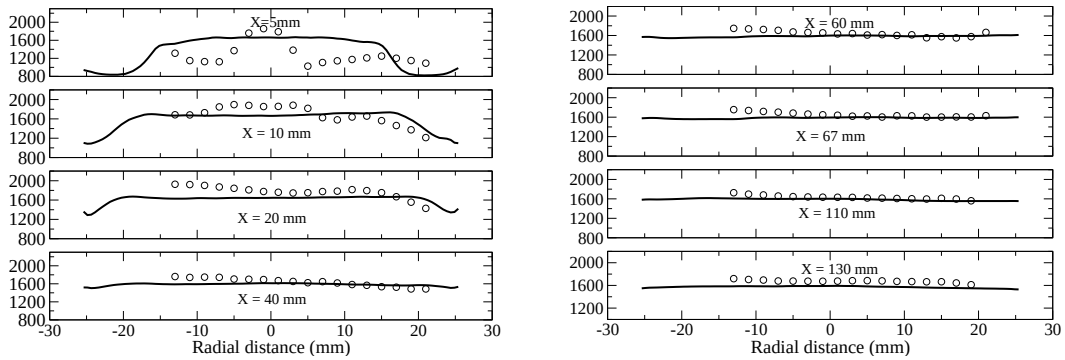

(a) $x = 5\,\text{mm}$-$x = 40\,\text{mm}$ (b) $x = 60\,\text{mm}$-$x = 130\,\text{mm}$

Fig. 20. Mean radial temperature profiles $\langle\, \overline{T}\, \rangle$ (Experiment $\circ$, computation $-$)

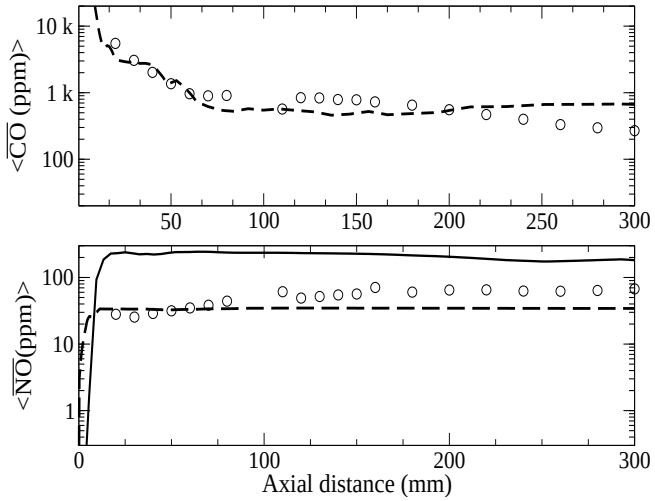

Fig. 21. Time averaged centerline species mass fractions profiles in ppm ($\langle \overline{Y}_{\mathrm{CO}} \rangle$ and $\langle \overline{Y}_{\mathrm{NO}} \rangle$) without radiation ($-$) and with radiation ($\cdot - \cdot$).

References

[1] A. H. Lefebvre, Gas Turbine Combustion, 2nd Edition, Taylor & Francis, London, UK, 1999.

[2] G. M. Faeth, G. Roth, M. Gundersen, Combustion emission and control., in: G. Roy (Ed.), Propulsion Combustion: Fuels and Emissions, Taylor & Francis, Washington, DC., 1998, pp. 359–407.

[3] I. Glassman, Proc. Combust. Inst. 22 (1988) 295 – 311.

[4] C. K. Law, Combustion Physcis, Cambridge University Press, New York, USA, 2006.

[5] S. J. Shanbhogue, S. Husain, T. Lieuwen, Prog. Energy Combust. Sci. 35 (1) (2009) 98–120.

[6] V. Sankaran, S. Menon, J. Turb. 2 (2002) 011.

[7] S. Menon, in: T. Lieuwen, V. Yang (Eds.), Combustion Instabilities in Gas Turbine Engines: Operational Experience, Fundamental Mechanisms, and Modeling, vol. 210, AIAA Progress in Aeronautics and Astronautics, 2005, pp. 277 – 314.

[8] S. Candel, J. Prop. Power 20 (1) (1988) 59 – 68.

[9] Pratt&Whitney, G. E. A. Engines, NASA/CR=2005-213584/VOL1.

[10] T. J. Poinsot, D. Veynante, Theoretical and Numerical Combustion, 2nd Edition, R. T. Edwards, Inc., Philadelphia, PA USA, 2005.

[11] C. K. Law, Proc. Combust. Inst. 31 (2007) 1 – 29.

[12] P. Pepiot-Desjardins, H. Pitsch, Combust. Flame 154 (1-2) (2008) 740 – 760.

[13] N. Peters, Proc. Combust. Inst. doi:10.1016/j.proci.2008.07.044.

[14] G. Boudiera, L. Y. M. Gicquela, T. J. Poinsot, Combust. Flame 155 (1-2) (2008) 196–214.

[15] M. Gorokhovski, M. Herrmann, Annu. Rev. Fluid Mech. 40 (2008) 343 – 366.

[16] O. Desjardins, H. Pitsch, J. Comput. Phys. doi:10.1016/j.jcp.2008.11.005.

[17] H. Watanabe, R. Kurose, S. Komori, H. Pitsch, Combust. Flame 152 (1-2) (2008) 2–13.

[18] S. B. Pope, Prog. Energy Combust. Sci. 11 (2) (1985) 119–192.

[19] N. Peters, Turbulent Combustion, Cambridge University Press, Cambridge, UK, 2000.

[20] H. Pitsch, Annu. Rev. Fluid Mech. 38 (2006) 233–266.

[21] H. Pitsch, O. Desjardins, G. Balarac, M. Ihme, 46^{th} AIAA Aerospace Sciences Meeting and Exhibit, Reno, Nevada, Jan. 7-10, 2008 AIAA-2008-604.

[22] N. Patel, S. Menon, Combust. Flame 153 (1) (2008) 228 – 257.

[23] H. El-Asrag, S. Menon, Proc. Combust. Inst. 31 (2007) 17471754.

[24] S. Menon, in: LES of Complex Transitional and Turbulent Flows, Kluwer Press, Dordrecht, 2000, pp. 329 – 352.

[25] J. C. Oefelein, V. Sankaran, T. G. Drozda, Proc. Combust. Inst. 31 (2) (2007) 2291 – 2299.

[26] V. Raman, H. Pitsch, Combust. Flame 142 (4) (2005) 329347.

[27] M. Boileau, G. Staffelbach, B. Cuenot, T. Poinsot, C. Brat, Combust. Flame 154 (1-2) (2008) 2–22.

[28] S. V. Apte, K. Mahesh, M. Gorokhovski, P. Moin, Proc. Combust. Inst., in press (2008) 10.10.16/j.proc.2008.06.156.

[29] L. Selle, G. Lartigue, R. Koch, K. U. Schildmacher, W. Krebs, P. Kaufmann, D. Veynante, Combust. Flame 137 (4) (2004) 489–505.

[30] J. Galpin, A. Naudin, L. Vervisch, C. Angelberger, O. Colin, P. Domingo, Combust. Flame 155 (1-2) (2008) 247–266.

[31] K.-S. Im, M. C. Lai, R. R. Tacina, 34^{th} AIAA/ASME/SAE/ASEE Joint Propulsion Conference and Exhibit, Cleveland, Ohio AIAA 1998-3269.

[32] R. R. Tacina, C. Wey, K. J. Choi, 37^{th} AIAA/ASME/SAE/ASEE Joint propulsion conference and Exhibit, Salt Lake City, Utah AIAA 2001-34065.

[33] S. L. Yang, Y. K. Siow, B. D. Peschke, R. R. Tacina, J. Eng. Gas Turbine Power 125 (2003) 804–811.

[34] J. Cai, S.-M. Jeng, R. R. Tacina, 43^{rd} AIAA Aerospace Sciences Meeting and Exhibit, Reno, Nevada AIAA 2005-1425.

[35] S. Honnet, K. Seshadri, U. Niemann, N. Peters, Proc. Combust. Inst. 32 (1) (2008) 485–492.

[36] H. Pitsch, Flamemaster, a c++ computer program for 0d combustion and 1d laminar flame calculations.

[37] C. D. Pierce, P. Moin, J. Fluid Mech. 504 (2004) 73 – 97.

[38] M. Ihme, C. M. Cha, H. Pitsch, Proc. Combust. Inst. 30 (1) (2008) 793 – 800.

[39] M. Ihme, H. Pitsch, Phys. Fluid 20 (2008) 0055110 – 20.

[40] G. L. Hubbard, C. L. Tien, Infrared mean absorption coefficients of luminous. flames and smoke, Heat Transfer 100 (1978) 235–239.

[41] S. V. Apte, M. Gorokhovski, P. Moin, Int. J. Multiphase Flow 29 (2003) 1503–1522.

[42] S. V. Apte, K. Mahesh, P. Moin, Proc. Combust. Inst., in press (2008) 10.10.16/j.proc.2008.05.058.

[43] F. Ham, in: Annual Research Briefs., Stanford Calif.: Center for Turbulence Research, 2007, pp. 41–45.

[44] D. Farhad, N.-S. Liu, P. M. Jeffrey, NASA/TM-2006-214252.

[45] A. C. Iannetti, N.-S. Liu, D. Farhad, NASA/TM-2008-215422.

[46] H. El-Asrag, F. Ham, H. Pitsch, in: Annual Research Briefs., Stanford Calif.: Center for Turbulence Research, 2007, pp. 241–253.

[47] N. Patel, M. Kirtas, V. Sankaran, S. Menon, Proc. Combust. Inst. 31 (2) (2007) 2327 – 2334.

List of Figures

REPORT DOCUMENTATION PAGE			Form Approved OMB No. 0704-0188

1. REPORT DATE *(DD-MM-YYYY)*	2. REPORT TYPE	3. DATES COVERED *(From - To)*
01-10-2011	Technical Memorandum	

4. TITLE AND SUBTITLE
Radiation-Spray Coupling for Realistic Flow Configurations

5a. CONTRACT NUMBER

5b. GRANT NUMBER

5c. PROGRAM ELEMENT NUMBER

6. AUTHOR(S)
El-Asrag, Hossam; Iannetti, Anthony, C.

5d. PROJECT NUMBER

5e. TASK NUMBER

5f. WORK UNIT NUMBER
WBS 984754.02.07.03.19.02

7. PERFORMING ORGANIZATION NAME(S) AND ADDRESS(ES)
National Aeronautics and Space Administration
John H. Glenn Research Center at Lewis Field
Cleveland, Ohio 44135-3191

8. PERFORMING ORGANIZATION REPORT NUMBER
E-17787

9. SPONSORING/MONITORING AGENCY NAME(S) AND ADDRESS(ES)
National Aeronautics and Space Administration
Washington, DC 20546-0001

10. SPONSORING/MONITOR'S ACRONYM(S)
NASA

11. SPONSORING/MONITORING REPORT NUMBER
NASA/TM-2011-217111

12. DISTRIBUTION/AVAILABILITY STATEMENT
Unclassified-Unlimited
Subject Categories: 07, 34, 64, and 28
Available electronically at http://www.sti.nasa.gov
This publication is available from the NASA Center for AeroSpace Information, 443-757-5802

13. SUPPLEMENTARY NOTES
Submitted to Journal of Combustion and Flame sponsored by Elsevier.

14. ABSTRACT
Three Large Eddy Simulations (LES) for a lean-direct injection (LDI) combustor are performed and compared. In addition to the cold flow simulation, the effect of radiation coupling with the multi-physics reactive flow is analyzed. The flame let progress variable approach is used as a subgrid combustion model combined with a stochastic subgrid model for spray atomization and an optically thin radiation model. For accurate chemistry modeling, a detailed Jet-A surrogate mechanism is utilized. To achieve realistic inflow, a simple recycling technique is performed at the inflow section upstream of the swirler. Good comparison is shown with the experimental data mean and root mean square profiles. The effect of combustion is found to change the shape and size of the central recirculation zone. Radiation is found to change the spray dynamics and atomization by changing the heat release distribution and the local temperature values impacting the evaporation process. The simulation with radiation modeling shows wider range of droplet size distribution by altering the evaporation rate. The current study proves the importance of radiation modeling for accurate prediction in realistic spray combustion configurations, even for low pressure systems.

15. SUBJECT TERMS
Combustion; Computational fluid dynamics; Thermal radiation; Turbulent flow; Sprays; Large eddy simulation (LES); Radiation; Lean-direct injection (LDI); Turbulent flames

16. SECURITY CLASSIFICATION OF:			17. LIMITATION OF ABSTRACT	18. NUMBER OF PAGES	19a. NAME OF RESPONSIBLE PERSON
a. REPORT	b. ABSTRACT	c. THIS PAGE			STI Help Desk (email:help@sti.nasa.gov)
U	U	U	UU	53	19b. TELEPHONE NUMBER *(include area code)* 443-757-5802